This is a preprint (available from http://mdolab.engin.umich.edu) of a conference paper submitted (22 June 2018) to the EngOpt 2018 conference.

Low-fidelity aerostructural optimization of aircraft wings with a simplified wingbox model using OpenAeroStruct

Shamsheer S. Chauhan(✉) and Joaquim R. R. A. Martins

University of Michigan, Ann Arbor, MI, USA
sschau@umich.edu

Abstract. It is common for aircraft design studies to begin with low-fidelity tools and move to higher-fidelity tools at later stages. After early conceptual design stages, designers can take advantage of developments in high-fidelity aerodynamic shape optimization, and more recently, coupled aerostructural optimization to improve their designs. Over the past few years, our research group has developed a framework that allows carrying out high-fidelity aerostructural optimization by coupling a RANS CFD solver to an FEM solver that uses shell elements. In addition, we have recently developed OpenAeroStruct, a light-weight and open-source tool for low-fidelity aerostructural optimization that couples a VLM code to an FEM code that uses spatial beam elements. Due to their low cost, such low-fidelity tools remain useful for design studies. In this paper, we present results from OpenAeroStruct for the optimization of a transport aircraft wing and compare them to results from our group's high-fidelity framework. Additionally, we describe the simplified wingbox model developed and implemented with OpenAeroStruct for this work.

Keywords: aerostructural, FEM, OpenAeroStruct, VLM, wingbox

1 Introduction

Due to their low cost, vortex lattice method (VLM) codes and simple finite element method (FEM) models remain popular and useful for preliminary aircraft wing design, despite the availability of higher-fidelity tools. Drela [1] used multiple tools including a VLM code and an aircraft design framework with simplified analytical structural models for the development of the D8 configuration, an unconventional transport aircraft configuration. Elham and van Tooren [2] coupled a quasi-3-D aerodynamics model, that combines a VLM code and a 2-D viscous solver, to an FEM code with beam elements. They optimize a wing based on the Airbus A320-200 with respect to shape, planform, and structural sizing variables [2]. Fujiwara and Nguyen [3] also coupled a quasi-3-D model, combining a VLM code and a 2-D viscous solver, to an FEM code with beam elements calibrated using a NASTRAN wing model for the structure. Their work

focuses on trailing-edge morphing and aerodynamic optimization to improve the performance of the common research model (CRM) [4] wing [3].

Unfortunately, these aerostructural design tools are not open-source or easily available to students and researchers. Recently, OpenAeroStruct[1] (OAS) [5], a low-fidelity tool for aerostructural optimization built using NASA's OpenMDAO[2] framework [6, 7], was developed to provide students and researchers with an open-source tool for studying coupled-aerostructural design trends. OAS couples a VLM model for the aerodynamics to an FEM spatial beam model for the structures.

Currently, OAS is gaining popularity with both students and researchers [5, 8–11]. However, one current limitation of OAS is that it models the structures as tubular spars. While this is useful for studying aerostructural coupling and optimization trends, a tubular cross-section is not representative of the wingbox structures commonly found in business, regional, and commercial aircraft.

To remedy this, and since no open-source software is available that couples a VLM code to an FEM code modeling a wingbox structure, we developed and present a modified version[3] of OAS with a wingbox model. To be specific, we modified the FEM analysis in OAS to use the effective properties of a simplified wingbox. To maintain the simplicity and light-weight nature of OAS, we still use six-degree-of-freedom-per-node spatial beam elements. However, we compute the effective cross-sectional properties for the elements using a wingbox model with an airfoil-based cross-section. We think students, instructors, and researchers will find this light-weight open-source tool to be useful for aircraft design studies.

2 Formulation

Typically, transport aircraft wings are designed with structures called wingboxes. The upper and lower wing skins primarily support the bending loads on the wing, and the two spars primarily support the shear loads. The skins and spars together also provide a closed loop for the torsional shear flow, allowing them to support torsional loads efficiently. This section describes how we model such a structure using beam elements.

As with the standard OAS, we use the same user-provided VLM meshes for both the VLM and the FEM. The FEM uses the spanwise spacing of the VLM mesh for the beam elements. Figure 1 illustrates an FEM mesh superimposed on a user-provided VLM mesh. The shaded boxes illustrate the segments of the wingbox structure that are represented by these FEM elements. For the FEM, section properties of these segments, for cross-sections normal to the elements, are required.

For each finite element that the wing structure is discretized into, the area moments of inertia about two axes, the torsion constant, and the cross-sectional area are required. We estimate these using user-specified wingbox coordinates,

[1] https://github.com/mdolab/OpenAeroStruct
[2] www.openmdao.org
[3] https://github.com/shamsheersc19/OpenAeroStruct/tree/mpt_wingbox

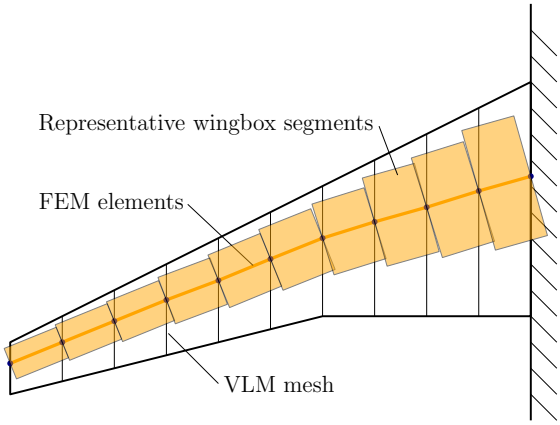

Fig. 1: A planform view of a wing mesh showing the VLM mesh and the FEM mesh with representative wingbox segments

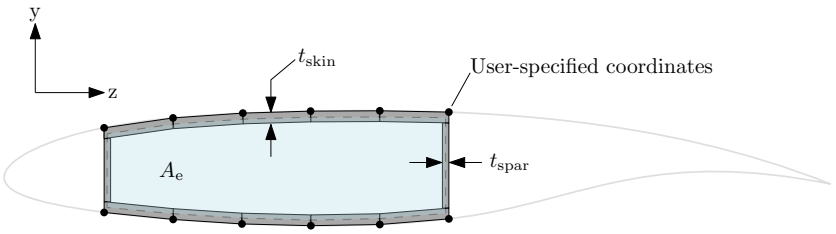

Fig. 2: The wingbox cross-section model is constructed using user-specified airfoil coordinates and the thickness design variables.

which are coordinates of the portion of the airfoil that the wingbox occupies (e.g., airfoil coordinates of the 15%- to 65%-chord portion of an airfoil). Figure 2 illustrates how the cross-section of each element is modeled using these coordinates.

The moments of inertia and area contributions of the skins are estimated using parallelograms formed by extruding the lines connecting the coordinates in the element's local y-direction by the skin thickness. The moments of inertia and area contributions of the spars are estimated using rectangles as shown in Fig. 2. For each wingbox segment, we use the same skin thickness, t_{skin}, for both the upper and lower skins, and the same spar thickness, t_{spar}, for both the forward and rear spars. Also, we compute the chord length for each segment by taking the mean of the chord lengths at its nodes.

2.1 Torsion Constant

For a closed section in which the wall thicknesses are much smaller than the other dimensions, the shear flow can be assumed to be uniform across the wall

thickness, and the torsion constant, J, can be approximated as [12]

$$J = \frac{4A_{\mathrm{e}}^2}{\oint \frac{\mathrm{d}s}{t}} \ . \tag{1}$$

Here, A_{e} is the enclosed area of the cross-section defined by the wall midlines, $\mathrm{d}s$ is the length of a differential element along the wall midlines, and t is the corresponding wall thickness.

We compute the enclosed area, A_{e}, for each cross-section by summing areas of trapezoids that together form the blue shaded region outlined by dashed lines in Fig. 2. We estimate the $\oint \frac{\mathrm{d}s}{t}$ term in Eq. (1) by computing the lengths of the dashed line segments shown in Fig. 2 divided by their corresponding thicknesses.

For transferring loads from the VLM to the FEM, we require the location of the shear center along the chord for each wingbox segment. If the wingbox cross-section has two axes of symmetry, then the shear center coincides with the centroid of the cross-section. However, in general, wingbox cross-sections are not symmetric, and finding the exact shear center of closed asymmetric cross-sections is an involved task [13]. To maintain simplicity, we estimate the location of the shear center along the chord as the average location of the outer edges of the spars, weighted by their areas. While there will be some error associated with this estimate, we expect this to be small, especially for typical wingbox cross-sections which are close to doubly symmetric.

2.2 Area Moments of Inertia

In general, the wing being optimized will have a variable twist distribution, and the wingbox sections will have some twist with respect to the local coordinate systems of the FEM elements, as illustrated in Fig. 3. To account for this, the user-specified wingbox coordinates are transformed as shown in Fig. 3. We achieve this by rotating the coordinates by the section's twist angle, and translating them such that the spars are aligned with the local y-axis. This assumes that the wing will be constructed with planar spar segments that are not twisted.

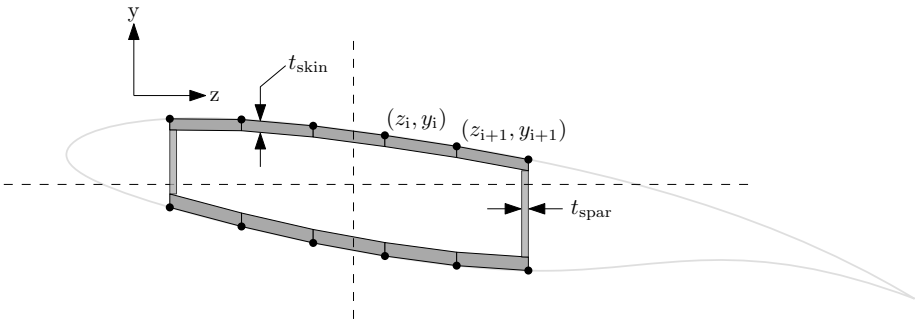

Fig. 3: Twisted wingbox cross-section

The area moment of inertia of each parallelogram on the upper skin about an axis passing through its centroid and parallel to the z-axis, I_{p}, is given by

$$I_{\mathrm{p}} = 2\left(\frac{a^3c^4}{12} + \frac{a^2bc^3}{3} + \frac{ab^2c^2}{2} + \frac{b^3c}{3}\right) , \tag{2}$$

where

$$a = \frac{y_{i+1} - y_i}{z_{i+1} - z_i},\ b = \frac{y_{i+1} - y_i + t_{\mathrm{skin}}}{2},\ \text{and}\ c = z_{i+1} - z_i\ . \tag{3}$$

We also compute the area moment of inertia of each parallelogram on the lower skin about their centroids using Eq. (2). However, the following modified formulas for a and b are required:

$$a_{(\mathrm{lower})} = -\frac{y_{i+1} - y_i}{z_{i+1} - z_i}\ \text{and}\ b_{(\mathrm{lower})} = \frac{-y_{i+1} + y_i + t_{\mathrm{skin}}}{2}\ . \tag{4}$$

Here, z_i, y_i, z_{i+1}, and y_{i+1} are consecutive user-specified wingbox coordinates as shown in Fig. 3. Then we use the parallel-axis theorem to adjust the moments of inertia calculated using the above formulas to moments of inertia about the neutral axis. For the contribution of the spars, we use the standard formulas for rectangular cross-sections.

Computing the area moment of inertia about the neutral axis parallel to the local y-axis is less involved and is carried out using the area moment of inertia formulas for a rectangle. Using the area moment of inertia formulas for a rectangle is also valid here for the parallelograms representing the skins because these parallelograms are simply rectangles sheared in the y-direction.

3 Loads

OAS transfers aerodynamic forces computed using the VLM to the FEM structure in a consistent and work-conservative manner [5]. For our modified version, we add additional loads for the weight of the wing structure and the weight of the fuel to these aerodynamic loads. For simplicity, we assume that the weight of the fuel is distributed across the entire wing and that the fraction of the total fuel that each wingbox segment (corresponding to each finite element) holds is equal to the ratio of its enclosed volume to the total enclosed volume of all the wingbox segments. We also assume that the fuel weight for each segment is distributed uniformly across each segment and coincides with the elastic axis. We apply these distributed loads as point loads to the nodes of the elements by computing the work-equivalent nodal forces and moments.

In a similar manner, we assume that the loads corresponding to the weight of each wingbox segment (computed using the length, cross-sectional area, and material density) are distributed uniformly along the elastic axis of each segment and apply them to the element nodes by computing the work-equivalent nodal forces and moments.

4 Stress Analysis

After OAS converges the aerostructural system, the displacements from the FEM are used to compute von Mises stresses. For each wingbox segment, multiple combinations of stresses need to be taken into consideration. In level flight and positive-g maneuver cases, the upper skin will be subjected to compressive stresses due to bending, and shear stresses due to torsion. The lower skin will be subjected to tensile stresses due to bending, and shear stresses due to torsion. The spars will primarily support shear stresses due to both torsion and shear loads, and some axial stresses due to bending. Figure 4 shows the stress combinations that we are interested in.

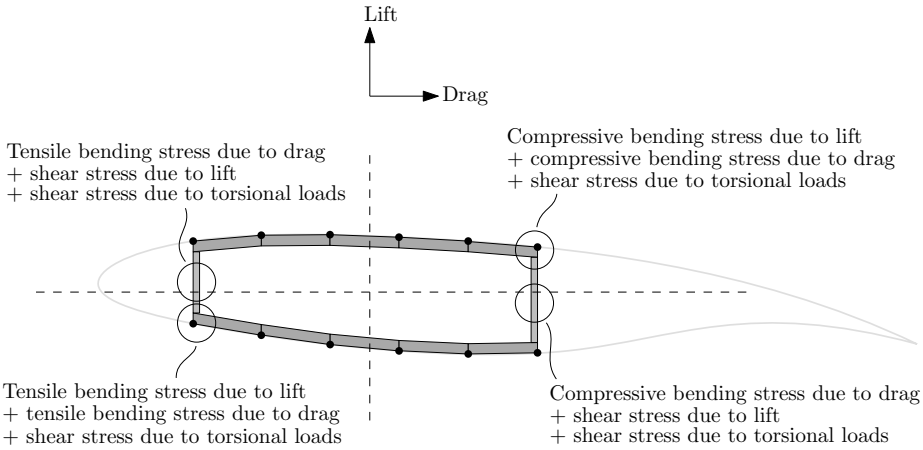

Fig. 4: Stress combinations of interest

To simplify the stress analysis, we focus on the four stress combinations shown in Fig. 4 to represent the worst loading combinations. To compute the maximum (in magnitude) bending stresses for the upper and lower surfaces, we need the distances of the points that are the farthest away from the neutral axis. Since this requires using a *maximum* function, which is problematic for gradient-based optimization, we use the Kreisselmeier–Steinhauser (KS) function [14]. To reduce numerical difficulties we use the alternative formulation described by Lambe et al. [15]. The bending stresses computed using these distances are combined with the maximum bending stresses in the spars, and the torsional shear stress to obtain a conservative estimate of the maximum von Mises stresses for the combinations corresponding to the corners in Fig. 4. Since we assume that the spars stay parallel to the local y-axis, computing their distances from the neutral axis is straightforward and does not require using a KS function. For the spars, we combine the maximum transverse shear stresses, the maximum bending stresses (due to loads in the local z-direction), and the torsional shear stress. After the

von Mises stresses are computed, we aggregate them using the KS function for a single stress constraint. Note that Fig. 4 is used for illustrative purposes and, in general, the lift and drag forces will not line up with the element local z- and y-directions.

5 Optimization Problem

One of the goals of this paper is to compare optimization results from OAS and our wingbox model to results from a framework that uses high-fidelity CFD and FEA. Brooks et al. [16] present optimization results for the aspect-ratio-9 undeflected common research model (uCRM-9) wing, which is an undeflected version of the CRM wing [4], a transport aircraft wing similar in size to a Boeing 777 wing. They use RANS CFD for the aerodynamics and an FEM model with shell elements for the wing structure [16, 17]. The objective of their optimization problem is to minimize fuel burn by varying aerodynamic shape and structural sizing variables. For a robust aerodynamic design, they compute their objective function by averaging the fuel burn for five cruise conditions (Mach numbers ranging from 0.84 to 0.86 and lift coefficients ranging from 0.475 to 0.525). In addition, they have two flight points for buffet constraints. For structural sizing, they use a 2.5 g maneuver case, a -1 g maneuver case, and a 1 g cruise gust case.

Their design variables include angle of attack, tail trim angle, wing twist, airfoil shape variables, and structural sizing variables. They model stiffeners for the wingbox using a smeared stiffness approach [18] and also include buckling constraints. They obtained an optimized wing structural mass of 23,840 kg and an average fuel burn of 94,037 kg.

We try to replicate their optimization problem closely for comparison. Table 1 lists the specifications and parameters used by Brooks et al. [16] that we also use for this work. We use a wing mesh, based on the uCRM-9 [17], with seven streamwise nodes and 26 spanwise nodes for the semispan (mesh shown in Fig. 5). Since we do not model a fuselage, the wings extend to the aircraft centerline.

Table 1: Parameters and specifications [16]

Specification	Value	Notes
Cruise range	7,725 nmi	
Cruise C_L	0.5	Nominal cruise lift coefficient
Cruise Mach no.	0.85	Brooks et al. use five cruise points, three of which are at M 0.85
Cruise altitude	37,000 ft	
Cruise thrust-specific fuel consumption	0.53 lb/lbf h^{-1}	
2.5 g maneuver Mach no.	0.64	
2.5 g maneuver altitude	0 ft	
Aircraft weight without wing structure, payload, and fuel	114,000 kg	
Payload weight	34,000 kg	
Reserve fuel weight	15,000 kg	
Drag counts for nacelles, pylons, and vertical tail	35	
Wing structure material density	2,780 kg/m^3	7000 series aluminum
Wing structure Young's modulus	73.1 GPa	7000 series aluminum
Wing structure Poisson's ratio	0.33	7000 series aluminum
Wing structure yield strength	420 MPa	7000 series aluminum

Table 2 summarizes our optimization problem. We use a multipoint optimization with a cruise flight point and a 2.5 g maneuver flight point. Minimizing the fuel burn at cruise is the objective and we use a single point at the nominal cruise C_{L}, altitude, and Mach number listed in Table 1 to compute it. We use the gradient-based optimizer SNOPT [19] to solve the optimization problem, with optimality and feasibility tolerances set to 5×10^{-6} and 10^{-8}, respectively.

Table 2: Optimization problem

	Function/variable	Note	Quantity
minimize	fuel burn	computed using the Breguet range equation	
with respect to	wing twist	B-spline parameterized using 6 control points	6
	thickness-to-chord ratio	B-spline parameterized using 6 control points	6
	spar thickness	B-spline parameterized using 6 control points	6
	skin thickness	B-spline parameterized using 6 control points	6
	angle of attack for the 2.5 g case		1
		Total design variables	**25**
subject to	$C_{\mathrm{L,cruise}} = 0.5$	for the cruise flight point	1
	$\mathrm{lift}_{2.5\,\mathrm{g}} = \mathrm{weight}_{2.5\,\mathrm{g}}$	for the 2.5 g maneuver flight point	1
	$\sigma_{\mathrm{von\,Mises}} \leq \frac{420\,\mathrm{MPa}}{1.5}$	von Mises stresses aggregated using the KS function	1
	fuel volume $\leq$ wingbox volume		1
		Total constraint functions	**4**

For structural sizing, we use a 2.5 g maneuver case with the lift constrained to equal the weight. We use B-splines with six control points each to vary the wing twist, streamwise thickness-to-chord ratio, spar thickness, and skin thickness. We use the same thickness distribution for both the upper and lower skins, and the same thickness distribution for both the forward and rear spars. The bounds for the wing twist, thickness-to-chord ratio, and thickness design variables are -15° and 15°, 0.07 and 0.2, and 0.003 m and 0.1 m, respectively.

Since we do not model the fuselage or tail surfaces, we estimate the unaccounted coefficient of drag for the fuselage and horizontal tail to be 0.0043. We used turbulent skin friction and form-factor formulas from Raymer [20], and the dimensions of the Boeing 777-200 for this. We further add a coefficient of drag of 0.0035 to this for the vertical tail, nacelles, and pylons (estimate used by Brooks et al. [16]). For the wingbox model used by Brooks et al. [16], at the root, the forward spar is located at the 10% chord location and the rear spar is located at the 60% chord location. At the wingtip, their forward spar is located at the 35% chord location and the rear spar is located at the 60% chord location. For simplicity, we set the forward spar to be at the 10% chord location and the rear spar to be at the 60% chord location for the entire wing. We use airfoil coordinates of the 10% to 60% portion of the NASA SC2-0612 supercritical airfoil for the wingbox cross-section shape. The thickness-to-chord ratio design variables scale these coordinates. Like Brooks et al. [16], for this optimization problem, we compute the weight of the wing structure by multiplying the weight computed from the FEM model by 1.25 to account for the weight of fasteners, overlaps, and other unaccounted components in the wing structure.

6 Results

Figure 5 shows our first set of optimization results. The lift distribution for the 2.5 g maneuver case is more triangular than the cruise case. This is expected because moving the lift further inboard for the 2.5 g case, which determines the structural sizing, is beneficial for reducing stresses and weight. We also observe a lower twist at the wingtip compared to the midspan and the root. This is expected as it helps obtain the optimal lift distributions. However, due to the different fidelities being used, there are differences in the shapes of the distributions in Fig. 5 and the optimized distributions obtained by Brooks et al. [16, 17]. For example, the thickness-to-chord ratios obtained by Brooks et al. [16] (for the uCRM-9) first decrease and then increase when moving from the root to the tip.

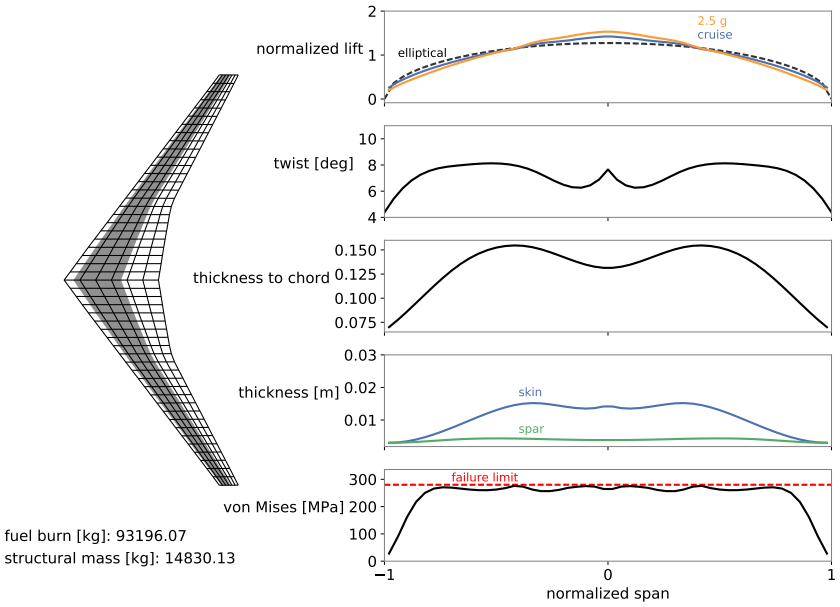

Fig. 5: Optimization results for the case without wave drag

The optimized thickness-to-chord ratios are relatively large for this case, between 0.12 and 0.16, in the midsection of each semispan. OAS computes induced drag from the VLM, and parasitic drag using skin friction and form-factor formulas found in Raymer [20]. However, wave drag, which is an important consideration for the design of transonic aircraft, is not included. This explains why we obtain these relatively large thickness-to-chord ratios. The optimized spar thicknesses range between 3 and 5 mm, and the optimized skin thicknesses range between 3 and 16 mm. Brooks et al. [16] obtained spar thicknesses between 5 and 16 mm, skin thicknesses between 3 and 22 mm, and thickness-to-chord ra-

tios between 0.07 and 0.11. Our optimized wing structural mass for this case is 14,830 kg. This is 38% lower than the optimized wing structural mass reported by Brooks et al. [16]. The large differences between our results can be explained by the larger thickness-to-chord ratios that the lack of wave drag allows.

Next, we add a wave-drag computation to OAS. We use the following relations [21] for the drag based on the Korn equation:

$$M_{\text{crit}} = \frac{\kappa}{\cos\Lambda} - \frac{t/c}{\cos^2\Lambda} - \frac{C_{\text{L}}}{10\cos^3\Lambda} - \left(\frac{0.1}{80}\right)^{1/3} \tag{5}$$

and

$$C_{\text{D,wave}} = 20(M - M_{\text{crit}})^4 \ . \tag{6}$$

Here, M is the flight Mach number, M_{crit} is the critical Mach number, κ is an airfoil-technology factor (set to 0.95 for NASA supercritical airfoils), t/c is the streamwise thickness-to-chord ratio, C_{L} is the wing coefficient of lift, and Λ is the sweep angle. We compute $\cos\Lambda$, by averaging the cosines of the quarter-chord sweep angles for each spanwise segment of the VLM mesh, weighted by their areas. Similarly, we compute the average thickness-to-chord ratio, t/c, by averaging the thickness-to-chord ratios corresponding to each spanwise segment, weighted by their areas.

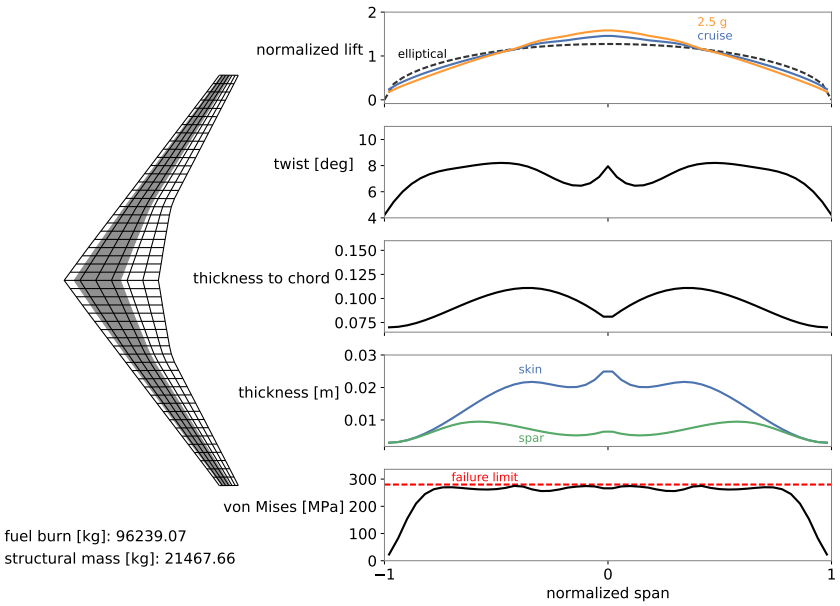

Fig. 6: Optimization results for the case with wave drag estimates

Figure 6 shows our optimization results including the wave drag computation. We notice similar results for the lift and twist distributions as the previous

Table 3: Optimized fuel burn and wing structural mass values (percentage differences relative to Brooks et al. [16] are shown in parentheses)

	OAS + wingbox		Brooks et al. [16]
	without wave drag	with wave drag	
Wing structural mass [kg]	14,830.13 (−38.8%)	21,467.66 (−10.0%)	23,840
Fuel burn [kg]	93,196.07 (−0.9%)	96,239.07 (+2.3%)	94,037

case. However, now we obtain a thinner wing (thickness-to-chord ratios between 0.07 and 0.12) with thicker spars (between 3 and 10 mm) and thicker skins (between 3 and 25 mm). These thickness ranges are closer to the ranges obtained by Brooks et al. [16] (spar thicknesses between 5 and 16 mm, and skin thicknesses between 3 and 22 mm). This also translates to a larger wing mass than before of 21,468 kg, which is 10% less than the wing mass of 23,840 kg obtained by Brooks et al. [16]. Note that these wing mass values are the masses computed from the wingbox structural models (combined total for both semispans) and do not include the 1.25 factor mentioned earlier. Since Brooks et al. [16] also consider buckling constraints and model ribs, which we do not, our lower wing mass is not surprising. These numbers are also comparable to the mass of 22,988 kg obtained by Klimmek [22] for the CRM using a doublet lattice method (DLM) code and a detailed FEM model. Our optimized fuel burn value is 96,239 kg, which is 2% greater than the fuel burn value of 94,037 kg obtained by Brooks et al. [16]. Table 3 summarizes the optimized fuel burn and structural mass values. Although these final values show good agreement, there are differences in the shapes of our optimized distributions and the results of Brooks et al. [16]. This is expected due to the differences in the fidelities of our models, and requires side-by-side comparison and further investigation to explain the details.

7 Conclusion

We developed a simplified wingbox model and implemented it for use with OpenAeroStruct. This modified version of OpenAeroStruct is open-source and publicly available. We optimized a wing based on the CRM wing and compared the results to results from Brooks et al. [16], who use high-fidelity models. Our optimized wing mass value is 10% lower and our optimized fuel burn value is 2% higher than their results. As expected due to the differences in the fidelities of our models, there are differences in the optimized twist, thickness-to-chord ratio, and structural thickness distributions. In contrast to 48 h on 1000 processors required by Brooks et al. [16], these optimizations with OpenAeroStruct require on the order of minutes to hours on a personal computer. We think students and researchers studying aircraft design will find this tool to be useful.

Acknowledgements. We would like to thank John Jasa for his support with OpenAeroStruct.

References

[1] Drela M (2011) Development of the D8 transport configuration. In: 29th AIAA Applied Aerodynamics Conference, American Institute of Aeronautics and Astronautics, doi:10.2514/6.2011-3970

[2] Elham A, van Tooren MJL (2016) Coupled adjoint aerostructural wing optimization using quasi-three-dimensional aerodynamic analysis. Structural and Multidisciplinary Optimization 54(4):889–906, doi:10.1007/s00158-016-1447-9

[3] Fujiwara GE, Nguyen NT (2017) Aeroestructural design optimization of a subsonic wing with continuous morphing trailing edge. In: 35th AIAA Applied Aerodynamics Conference, American Institute of Aeronautics and Astronautics, doi:10.2514/6.2017-4218

[4] Vassberg JC, DeHaan MA, Rivers SM, Wahls RA (2008) Development of a common research model for applied CFD validation studies. doi:10.2514/6.2008-6919, aIAA 2008-6919

[5] Jasa JP, Hwang JT, Martins JRRA (2018) Open-source coupled aerostructural optimization using Python. Structural and Multidisciplinary Optimization 57:1815–1827, doi:10.1007/s00158-018-1912-8

[6] Gray J, Hearn T, Moore K, Hwang JT, Martins JRRA, Ning A (2014) Automatic evaluation of multidisciplinary derivatives using a graph-based problem formulation in OpenMDAO. In: Proceedings of the 15th AIAA/ISSMO Multidisciplinary Analysis and Optimization Conference, Atlanta, GA, doi:10.2514/6.2014-2042

[7] Hwang JT, Martins JRRA (2018) A computational architecture for coupling heterogeneous numerical models and computing coupled derivatives. ACM Transactions on Mathematical Software (In press)

[8] Peherstorfer B, Beran PS, Willcox KE (2018) Multifidelity Monte Carlo estimation for large-scale uncertainty propagation. In: 2018 AIAA Non-Deterministic Approaches Conference, American Institute of Aeronautics and Astronautics, doi:10.2514/6.2018-1660

[9] Tracey BD, Wolpert D (2018) Upgrading from Gaussian processes to Student's-t processes. In: 2018 AIAA Non-Deterministic Approaches Conference, American Institute of Aeronautics and Astronautics, doi:10.2514/6.2018-1659

[10] Chaudhuri A, Jasa J, Martins JRRA, Willcox K (2018) Multifidelity optimization under uncertainty for a tailless aircraft. In: 2018 AIAA/ASCE/AHS/ASC Structures, Structural Dynamics, and Materials Conference; AIAA SciTech Forum, Orlando, FL, doi:10.2514/6.2018-1658

[11] Chauhan SS, Hwang JT, Martins JRRA (2018) An automated selection algorithm for nonlinear solvers in MDO. Structural and Multidisciplinary Optimization doi:10.1007/s00158-018-2004-5, (In press)

[12] Beer FP, Jr ERJ, DeWolf JT, Mazurek DF (2014) Mechanics of Materials, 7th Edition. McGraw-Hill Education

[13] Grant C (1992) Shear centre of thin-walled sections. The Journal of Strain Analysis for Engineering Design 27(3):151–155, doi:10.1243/03093247v273151

[14] Kreisselmeier G, Steinhauser R (1979) Systematic control design by optimizing a vector performance index. In: International Federation of Active Controls Symposium on Computer-Aided Design of Control Systems, Zurich, Switzerland, doi:10.1016/S1474-6670(17)65584-8

[15] Lambe AB, Martins JRRA, Kennedy GJ (2017) An evaluation of constraint aggregation strategies for wing box mass minimization. Structural and Multidisciplinary Optimization 55(1):257–277, doi:10.1007/s00158-016-1495-1

[16] Brooks TR, Kenway GKW, Martins JRRA (2017) Undeflected common research model (uCRM): An aerostructural model for the study of high aspect ratio transport aircraft wings. In: 18th AIAA/ISSMO Multidisciplinary Analysis and Optimization Conference, Denver, CO, doi:10.2514/6.2017-4456

[17] Brooks TR, Kenway GKW, Martins JRRA (2018) Benchmark aerostructural models for the study of transonic aircraft wings. AIAA Journal doi:10.2514/1.J056603, (In press)

[18] Kennedy GJ, Kenway GKW, Martins JRRA (2014) High aspect ratio wing design: Optimal aerostructural tradeoffs for the next generation of materials. In: Proceedings of the AIAA Science and Technology Forum and Exposition (SciTech), National Harbor, MD, doi:10.2514/6.2014-0596

[19] Gill PE, Murray W, Saunders MA (2005) An SQP algorithm for large-scale constrained optimization. Society for Industrial and Applied Mathematics 47(1), URL http://www.stanford.edu/group/SOL/papers/SNOPT-SIGEST.pdf

[20] Raymer DP (2006) Aircraft Design: A Conceptual Approach, 4th edn. AIAA

[21] Malone B, Mason W (1995) Multidisciplinary optimization in aircraft design using analytic technology models. Journal of Aircraft 32(2):431–438, doi:10.2514/3.46734

[22] Klimmek T (2014) Parametric set-up of a structural model for fermat configuration aeroelastic and loads analysis. Journal of Aeroelasticity and Structural Dynamics 3(2):31–49, doi:10.3293/asdj.2014.27